COSMOLOGY, GRAVITATION, ASTROPARTICLE PHYSICS, HIGH ENERGY PHYSICS

https://doi.org/10.18524/1810-4215.2025.38.340287

A NOVEL IMAGE RECONSTRUCTION APPROACH IN THE X- AND γ-RAY DOMAIN

Dmitri Doikov[1], Katrin Doikova[2]

[1] Dept. of Physics, Medical Laboratory at Baruch Padeh Medical Center, Poriya, Israel, *dmitro.doikov@gmail.com*

[2] Dept. of Radiology, Baruch Padeh Medical Center, Poriya, Israel, *doikovaekaterin@gmail.com*

ABSTRACT. This study examines the consequences of high-energy radiation interactions from X-ray sources with extended astrophysical objects. A comparative analysis is conducted between the spectra of primary radiation sources and those of irradiated absorbing and scattering regions. The limitations of current diagnostic methods are identified, and strategies for enhancing both the sensitivity and informational value of the resulting data are proposed. Signal-to-noise ratios are derived for a gamma-ray detector prototype developed by the authors, under various geometric configurations of emitting and scattering structures. Necessary modifications to the radiation transport equations are suggested, along with instrumental techniques for identifying and registering previously unrecognized astrophysical entities.

Keywords: X-ray spectroscopy and detectors, visualization of chemical anomality's in X-rays, regularization algorithm, Compton spectroscopy.

АНОТАЦІЯ. У роботі розглянуто наслідки взаємодії жорсткого рентгенівського та гамма-випромінювання з протяжними астрофізичними об'єктами та середовищами різної природи. Проведено порівняння спектрів первинного випромінювання з характеристиками поглинаючих і розсіювальних областей, що піддаються опроміненню. Показано, що реконструкція зображень середовищ, які зазнають опромінення, та їх спостереження у прямих і розсіяних компонентах випромінювання потребують нових фізичних підходів, спеціалізованих інструментальних рішень і вдосконалених алгоритмів обробки даних.

Обґрунтовано необхідність використання інформаційного потенціалу розсіяного випромінювання. Доведено, що, всупереч поширеній думці про втрату якості та виникнення спотворень у детектованих проекційних зображеннях опромінюваних об'єктів μ(x, y) та μ(x, y), існують спектральні діапазони, де домінують «чисті» фізичні процеси: поглинання (0,1–10 кеВ) або розсіяння (40–160 кеВ). У проміжному енергетичному інтервалі 10–40 кеВ ці процеси конкурують. Для підвищення наочності та зручності аналізу було обрано рідкі та тверді фази найбільш поширених середовищ: для атмосфер планет – воду та метан, для міжзоряного середовища – тверді силікати й карбонати. Показано, що за діючої концентрації атомів, визначеної відповідно до формули (6), ще можливе використання наближення однократного розсіяння. Доведені можливості реконструкції проекцій $\mu_s(x, y)$ у розсіяному випромінюванні дозволяють охоплювати значно більший за геометричними та фізичними характеристиками об'єм простору. Цей ефект було зафіксовано космічними апаратами на енергіях, де превалює «чисте» поглинання. У таких умовах агентами розсіяння рентгенівського випромінювання є нано-частинки силікатів і карбонатів. Водночас характер розсіяння має дифракційну природу і визначається макроскопічними параметрами пилу, зокрема коефіцієнтом заломлення у рентгенівському діапазоні, який практично дорівнює одиниці.

На основі проведеного аналізу отримано співвідношення сигнал/шум для розробленого авторами детектора гамма-випромінювання за різної геометрії випромінювальних і розсіювальних об'єктів. Запропоновано необхідні модифікації рівнянь переносу та інструментальні методи ідентифікації й реєстрації раніше неідентифікованих об'єктів, що підвищує чутливість та інформативність отримуваних діагностичних даних.

Ключові слова: рентгенівська спектроскопія та детектори, візуалізація хімічних аномалій у рентгенівських променях, алгоритм регуляризації, комптонівська спектроскопія.

1. Introduction

Recent advances in astronomical observations, particularly the discovery of numerous X-ray sources, have opened new avenues for investigating the radiative response of the environments in which these sources are embedded. These environments are typically rarefied interstellar structures composed predominantly of gas and dust. Notable examples include young supernova remnants and active galactic nuclei (AGN). Within the Solar System, analogous media are represented by aerosols in the upper layers of planetary atmospheres,

containing particles of diverse chemical composition subjected to interactions with the high-energy component of cosmic rays. The problem of reconstructing cosmic structures was first introduced in the context of processing radioastronomical images (Bracewell & Riddle, 1967). The data recorded by detector elements (e.g., antennas) correspond to two-dimensional projections of three-dimensional spatial objects located within the radiation field. For subsequent analysis, such projections are denoted by the function *f(x, y)*. The diversity of geometrical configurations of both the radiation sources and the irradiated media enables the extraction of new information on the physical properties of these interacting systems. In laboratory settings, studies in the soft X-ray range are often hindered by the predominance of photoabsorption over scattering processes. Consequently, spectral analysis of spatially distributed objects relies primarily on the registration of the photoelectric effect and the resulting characteristic emission from the irradiated medium. Notably, redistribution of spectral intensities is observed only for allowed transitions to K-shells of atoms starting with beryllium (Jerkstrand et al., 2011). A key objective is to determine the minimum contrast of inhomogeneities required to resolve structural details at a given signal-to-noise ratio. It is observed that, for certain astrophysical objects, the peak of the X-ray energy distribution shifts toward higher energies. This behavior is typical for phenomena such as nova outbursts and X-ray sources, including pulsars in binary star systems. Among the non-compact sources, young supernova remnants–such as SNR 1987A–exhibit radiation from both forward and reverse shock fronts, as well as from radioactive decay of residual material. Emission from active galactic nuclei (AGN) also remains a subject of considerable interest.

In all the aforementioned cases, the radiation transport equation must be supplemented by an integral term accounting for the contribution of scattering. Cross-sections for photoabsorption and scattering across various media types are presented in detail in several previously published studies [see references]. In dense media where multiple scattering events are prominent, the impact of these processes on the stability and accuracy of image reconstruction procedures has been critically analyzed. The present study is restricted to the energy range covered by all modern X-ray observatories, with the exception of *Fermi LAT*, and therefore does not consider photon energies exceeding 10 MeV. Additionally, all radiation sources under consideration are associated with thermonuclear processes, which yield photon energies limited to a few MeV. The structure of the article is as follows. Section 1 provides a general introduction to the problem and the formulation of the research objectives. Section 2 outlines and analyzes the fundamental equations governing X-ray radiation transport in highly absorbing media, with particular focus on the characteristics of atomic emission that constitute the radiative response of the medium. Section 3 is devoted to the formation of detector-plane images f(x, y), incorporating the effects of multiple scattering. Section 4 presents methodologies for reconstructing the original spatial structure of the object from the recorded projections f(x, y). The Discussion offers an interpretation of the results and proposes directions for the development of third-generation spectrographic detectors based on the findings of this work. The Conclusion summarizes the key outcomes, compares the derived detector characteristics with those of first- and second-generation instruments, and highlights the relevance of spectral color indices for probing the chemical state of scattering media.

2. Radiation Transport Equations for X-rays

A key distinction between the interaction of high-energy radiation fields and matter–compared to interactions in optically active media–is the dominance of photoionization (i.e., the atomic photoelectric effect) in the soft X-ray range. In this regime, the process can be described as pure absorption. In the intermediate energy range, approximately from 30 to 130 keV, the photoabsorption cross-section decreases significantly, and beyond a certain energy threshold, Compton scattering becomes the predominant interaction mechanism. In physical media with average photon energies between 30 and 60 keV, multiple scattering events may occur. As photon energy increases further, the Compton scattering cross-section declines, and the probability of single scattering becomes dominant. Taking these phenomena into account, X-ray spectroscopy enables the formation of radiographic images and spectral projections of the irradiated objects. The same principles apply to the gamma-ray domain. Fig. 1 presents a comparative overview of modern space-based telescopes and the energy ranges covered by their respective spectroscopic instruments.

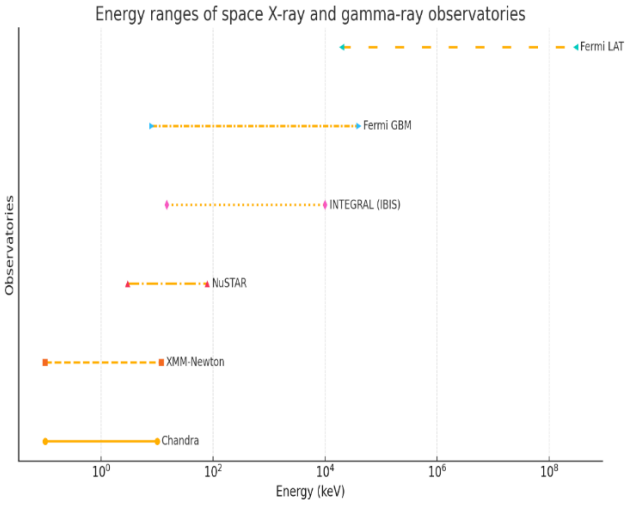

Figure1: Energy range of X- and γ-ray telescopes.

2.1. Physical Characteristics of Matter under High-Energy Radiation Exposure

Let us consider the line integrals of X-ray attenuation through the object.

$$p\ \theta,s\ =\ \int_{-\infty}^{+\infty} f\ x,y\ \delta\ s-x\cdot cos\theta-y\cdot sin\theta\ dxdy, \quad (1)$$

here, f(x, y) denotes the extinction coefficient distribution, while p(θ, s) is its projection–commonly referred to as a sinogram. Reconstruction of f(x, y) is performed using the inverse Radon transform (Yebb, 1989), (Bracewell & Riddle, 1967). In the ideal case:

$$f(x,y)=\int_0^{\pi}\int_{-\infty}^{+\infty} p\ \theta,\omega\ \omega e^{2\pi i\omega t\ s-x\cdot cos\theta-y\cdot sin\theta}\ d\omega\ \ d\theta\ . \quad (2)$$

In practical applications, the filtered back-projection method is used. Prior to its implementation, however, the scattering indicatrix describing X-ray interactions with atomic constituents of the medium must be introduced. Accordingly, the radiative transfer equation is reformulated in a more general framework, with particular emphasis on the geometric features of the target structures.

$$\frac{\mathrm{dI\ r,\Omega}}{\mathrm{ds}}=-\mu_t\ \mathrm{E,r\ I\ r,\Omega}\ +\ \int_{\mathbf{0}}^{\mathbf{4\pi}} 4\pi\mu_s\ \mathrm{E,r\ p_{KN}}(\Omega'\rightarrow\Omega)\mathrm{I}(\mathrm{r},\Omega')\mathrm{d}\Omega'\ . \quad (3)$$

The total attenuation coefficient is given by $\mu_t=\mu_a+\mu_s$, where μ_a,μ_s denotes the photo absorption and Compton scattering coefficient, and $\mathrm{p_{KN}}(\Omega'\rightarrow\Omega)$ is the Klein–Nishina indicatrix describing the angular probability distribution of scattered photons, normalized over the full solid angle 4π. Physically, this quantity expresses the probability of scattering into a direction defined by the angle θ

$$p_{KN}\ \ \theta\ =\frac{1}{\sigma_{KN}}r_e^2\ \ \frac{E'}{E}\ ^2\ (\frac{E'}{E}+\frac{E}{E'}-sin^2\theta\ )\ , \quad (4)$$

here, E' denotes the energy of the scattered quantum, while σ_{KN} represents the total Klein–Nishina cross-section for a single electron.

$$E'=E/(1+\frac{E_e}{m_ec^2\ 1-cos\theta})\ . \quad (5)$$

The radiation intensity $\mathrm{I\ r,\Omega}$ detected by the observer as a result of single scattering on spherical irregularities V_{irreg} with radius a can be expressed as

$$I_s\ \Omega_s\ \approx I_0\mu_s\ E\ \ \frac{V_{irreg}}{4\pi R_s^2}\cdot \mathrm{p_{KN}}(\theta_s)\ e^{-\mu_t(s_1+s_2)}\ . \quad (6)$$

The value $I_0\mu_s\ E\ \ \frac{V_{irreg}}{4\pi R_s^2}$ in equation (5), this quantity is equivalent to the density of scattering electrons, ρ_e, which is correlated with the average mass density of the medium. s_1,s_2 denote the distances from the source to the scattering object and from the object to the observer, respectively. The radiative transfer equation (3) is valid under the assumption of single scattering. To justify the applicability of this approximation, we estimate the mean free path l of an X-ray photon in water. To account for the actual contribution from oxygen atoms, we subtract their effect and retain the effective mean free path for hydrogen atoms alone. Assuming a representative value of $l\approx 8$ cm for X-rays with average energy, we obtain the mean effective number of atoms N_A.

$$N_A=2\cdot\frac{1}{9}\frac{\rho}{\mu_H}N_A\approx 8{,}058\cdot 10^{23}\ cm^{-2}. \quad (7)$$

For most rarefied astrophysical media and the upper layers of the Earth's atmosphere, such an approximation is acceptable. In the following section, we compare scattering degrees derived from modeling with those obtained using this approximation. Having determined N_A, we proceed to the geometry of the inhomogeneities under investigation and relate the scattered radiation from the source to the spatial distribution of average electron density within these structures. It is necessary to select a suitable function $f_s(x,y)$ analogous to the attenuation function, which can be reconstructed from the scattered photons. To do so, we must return to the fundamental question: what physical quantity is actually measured when scattering dominates? If the cone of unscattered (ballistic) rays intersects the observer's detector, then even in scattering-dominated regimes, we simultaneously record attenuation of the primary beam–described by the first term in Equation (3), $I_{prim}\ (\theta,s)$ –and the intensity of the scattered component, $I_{scat}\ \theta,s$, The latter is further refined by specifying the kernel of the double integral:

$$\begin{aligned} I_{prim}\ \ \theta,s\ &=I_0\ exp[-\int\mu\ x,y\ dl]\\ I_{scat}\ (\theta,s)&=\iint f_s\ (x,y)\ P(\psi(x,y\rightarrow s))\ \frac{1}{R^2}\ dxdy \end{aligned} \quad (8)$$

The function $f_s\ (x,y)$ represents the local electron density, i.e., the number of Compton-scattering centers. The angular distribution of scattered photons is described by the indicatrix $P\ \psi\ x,y\rightarrow s\ \ =p_{KN}\ \ \theta$ derived from the Klein–Nishina (KN) theory. Here, R denotes the distance from the scattering point to the detector. The corresponding expression involves a double integral taken over the entire volume of the medium. The scattered signal thus constitutes a convolution-type integral. In the absence of scattering and under dominant photo absorption, the kernel of the direct Radon integral along the ray connecting the primary radiation source and the observer's detector contains a delta function of the form $\delta\ s-x\cdot cos\theta-y\cdot sin\theta$. Numerical results illustrating scattering irregularities, including chemical composition anomalies, are shown in Fig. 3 for a hydrogen–oxygen medium with localized oxygen deficiency. Notably, when the magnitude of the anomaly falls below 3%, the scattered signal becomes indistinguishable from the noise level of the detection system. The energy of the incident photons is 130 keV.

2.2. The Role of Fluorescent X-ray Emission

Essentially, when photo absorption occurs in a gas–dust diffuse medium within the energy range up to 30 keV, all constituent elements with atomic numbers from 1 to 4

undergo only ionization, followed by the capture of free electrons from the medium and subsequent recombination through three-body collisions. The probability of such events in a diffuse environment is extremely low. A rare exception is found in young, dense supernova remnants, where the presence of metals in the inner layers can lead to an increase in electron density [Chevalier & Fransson, 2016). In such cases, photo absorption in elements starting from boron and above results in the formation of K-shell vacancies, the emission of high-energy electrons, and Auger electrons. The filling of K-shell vacancies gives rise to soft X-ray secondary radiation, which is efficiently reabsorbed in the surrounding medium. Therefore, the detection of such quanta provides a means for diagnosing the outer layers of the observed objects. The energy intervals between the absorption edges of these photons are referred to as transparency windows. Visualization of images within these 'windows' enables the characterization of deeper layers through the continuous component of the spectrum. The thermalization of X-ray radiation primarily begins with multiple Compton scatterings, followed by a cascade of energy loss and subsequent photo absorption.

3. The Multiple Scattering Approximation

Multiple scattering of X-ray radiation contributes to two principal effects. First, it reduces the contrast of the contours of observed structures in direct transmission images. On the other hand, in the absence of absorption in equation (3), contrast enhancement relative to the background noise emerges in regions of structural irregularities, as illustrated in Fig. 2. In other words, multiple scattering of X-ray photons gives rise to a diffuse component of the radiation field, which is a fundamental characteristic of the multiple scattering regime. This occurs because the quantities $P\ \psi\ x,y \to s\ \ = p_{KN}\ \ \theta$, derived from equations (3) and (4), can no longer adequately describe the entire scattering system as a whole. In such cases, the Monte Carlo method is employed to address the problem.

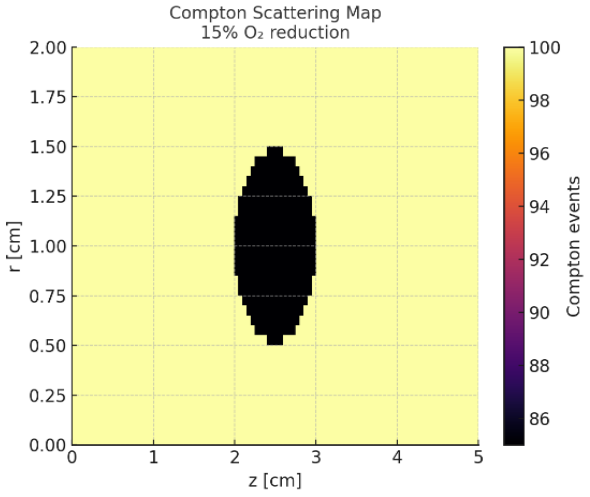

Figure 2: Spatial structure of the X-ray scattering region.

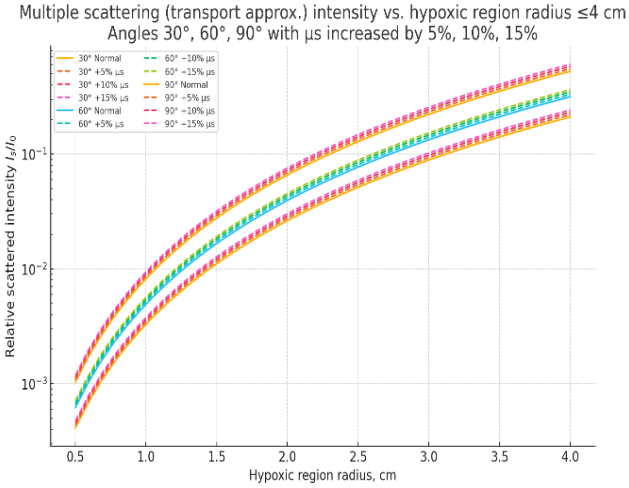

Figure 3: Experimental modeling of multiple scattering in oxygen-deficient liquid environments. The word hypoxic means the oxygen deficiency.

Fig. 3 plots showing scattering angles of 30°, 60°, and 90° under conditions of multiple scattering (transport approximation) for oxygen-deficient regions with radii ranging from 0.5 to 4 cm. At 30°, the intensity level is higher than at 60° and 90° due to the anisotropy of scattering. A 10–15% increase in the scattering coefficient μ_s (x, y) is observed with decreasing oxygen concentration in water, resulting in a noticeable contrast deviation for radii larger than 2 cm. For small regions (less than 1 cm), such differences remain undetectable.

4. Image Reconstruction from X-ray and Gamma-Ray Detector Readings

The inverse problem consists in reconstructing the geometry of a scattering region based on the radiation measured by detectors. The raw data (e.g., in the form of RAW files) are used for the visualization of objects via scattered radiation, a technique known as *scatter imaging*. The key idea is to reconstruct local variations in the attenuation coefficient μ_a (x, y) and the scattering coefficient μ_s (x, y) within the scattering region by analyzing the angular distribution and intensity of lateral scattering. To derive the relations required for solving the inverse problem, we rewrite the second (scattering) term in equation (3) in a more convenient form:

$$I_s\ \ \theta, r_d\ \ = \int_0^V G\ r, r_d, \theta\ \ \mu_s\ \ r\ \ \Phi\ r\ \ dV\,. \qquad (9)$$

Where $\Phi\ r$ denotes the primary radiation fluence at point r, associated with the local scattering coefficient $\mu_s\ \ r$, and $G\ r, r_d, \theta$ is a geometric and transport operator that accounts for attenuation, the scattering indicatrix $p_{KN}\ \ \theta$ and the propagation path to the detector. The measurement process represents a discrete data acquisition scheme, in which the detector readings are recorded in sampled form. In the presence of mmm detector channels, each channel must be mapped to its corresponding angular and spatial coordinates:

$$I_m^{meas} = \ {}_j K_{mj}\ \mu_{s,j} + noise\ . \quad (10)$$

Where K_{mj} is the sensitivity matrix (kernel), $\mu_{s,j}$ is the parameter to be estimated–representing spatial variations of the scattering coefficient μ_s , and *noise* denotes statistical measurement noise.

4.1. Inverse Problem Statement

It is required to determine the fields $\boldsymbol{\Delta\mu_s}\ (\boldsymbol{r})$, that give rise to anomalies in the scattering intensity.

$$\Delta I_m = \ {}_j K_{mj}\ \Delta\ \mu_{s,j} \quad (11)$$

Which corresponds to the solution of a linear inverse problem.

$$\Delta I = K \cdot \Delta\ \mu_s\ . \quad (12)$$

Structure of the Raw Data from Detectors. In X-ray detectors, pixels are arranged in the form of a square matrix, whose dimensions are determined by the manufacturer. Each detector is associated with a two-dimensional matrix and corresponding time series that record the activation time of each pixel following the interaction with an X-ray photon. This structure enables dynamic monitoring of the imaged objects. In classical detectors of the first and second generations, image analysis and reconstruction rely primarily on object projections formed by photon absorption. It is generally assumed that this is sufficient for reconstructing the density distribution of the object. In contrast, our method utilizes projections formed by X-rays scattered by atomic electrons within the object. As shown in Fig. 5 from (Doikov D & Doikov M, 2024), there exists a spectral region in which scattering dominates over photoabsorption.

4.2. Reconstruction Methods

The reconstruction of astronomical images was first introduced in the late 1960s in the context of radio interferometric observations. The primary objective of these studies was to determine the geometric and physical characteristics of observed objects. By comparing regions responsible for absorption and scattering of radio waves during data processing, it became possible to achieve the necessary image contrast. A subsequent development involved obtaining high-contrast optical and infrared images containing fine structural details in planetary atmospheres within the Solar System. In this case, the recorded radiation was affected by Rayleigh molecular scattering. The variation in measured scattered radiation as a function of planetary rotation enabled the association of signals with the angular coordinate θ. Once the intensity distribution of scattered radiation was obtained, a suitable image reconstruction method could be selected. Currently, the following reconstruction approaches are widely used:

1. **Algebraic Methods (ART, SIRT).** A response matrix K is constructed (e.g., via Monte Carlo simulation for a given anomalous medium), and a minimum-norm solution is obtained using a regularization parameter λ:

$$\Delta\mu_s = \arg\ min \parallel K\Delta\mu_s - \Delta I \parallel^2 + \lambda \parallel \Delta\mu_s \parallel . \quad (13)$$

2. **Iterative Reconstruction with Regularization**. Используется Maximum-Likelihood Expectation Maximize**.** An advanced class of reconstruction techniques employs iterative schemes with embedded regularization. One widely used algorithm is Maximum-Likelihood Expectation Maximization (MLEM)**,** which is particularly effective in low-photon-count or Poisson-limited regimes. The algorithm iteratively updates the estimate of the scattering or attenuation distribution μ(r) to maximize the likelihood of observing the measured detector data, while optional regularization terms may be included to stabilize the solution and suppress noise action (MLEM).

3. **Diffusion Approximation / Transport Model Fit.** The scattering process is modeled using a diffusion approximation or a full radiative transport model, with spatially varying parameters $\Delta\mu_s$ and $\Delta\mu_a$ in different regions. The model parameters are adjusted so that the simulated lateral (scattered) signal matches the experimentally measured data. This approach is particularly suitable when multiple scattering dominates and the medium can be approximated as diffusive.

4.3. Stepwise Reconstruction Algorithm

- Data preparation: Convert RAW data into sinograms as a function of projection angle; normalize with respect to angle and photon energy.
- Model calibration: Select a precomputed or experimentally calibrated model using a reference sample to obtain the system response matrix K. Subtract the background signal (scattering from the entire nominal model without anomalies).
- Optimization and inversion: Perform data inversion and parameter estimation using equation (13) in combination with Algebraic Reconstruction Techniques (ART/SIRT) augmented with Total Variation (TV) or Tikhonov regularization.
- Interpretation: Analyze the reconstructed image to obtain a spatial map of $\Delta\mu_s\ (r)$ .representing local deviations in the scattering coefficient.
- Noise suppression and structural enhancement: The highest image quality and feature resolution are achieved using TV regularization, which effectively suppresses noise and reconstructs smoothed or piecewise-constant anomalies:

$$min_x \parallel Kx - \Delta I \parallel^2 + \lambda\, TV(x)\ . \quad (14)$$

Depending on the nature and characteristics of the measured data, two forms of total variation (TV) regularization can be applied:

Anisotropic or simple form: the absolute differences between neighboring pixel (voxel) values are summed separately along the horizontal and vertical directions. At

this stage, artifacts and noise in the projection signals are partially suppressed.

$$TV\ x\ =\ _{i,j}\ x\ i+1,j\ -x\ i,j\ \ +\ x\ i,j+1\ -\ x\ x\ i,j \tag{15a}$$

Isotropic form: enables smoothing of sharp discontinuities and artifacts that may occur during image acquisition on the detector.

$$TV\ x\ = \ _{i,j}\ \sqrt{x\ i+1,j\ -x\ i,j\ ^{2}+\ x\ i,j+1\ -x\ i,j\ ^{2}} \tag{15b}$$

Here, the gradient is computed at each pixel (in both x and y directions), its norm is taken, and then the result is summed over the entire domain. The first term in equation (14) is based on comparison and alignment with the measured data, while the second term suppresses excessive oscillations. As a result, the solution becomes piecewise constant and more effectively reveals localized anomalies. These anomalies constitute the main objective of the present study. Essentially, by anomalies we refer to rapid lightning formation and various energy bursts occurring under terrestrial and cosmic conditions.

5. Calculation Results

Many problems in astrophysics and planetary astronomy are based on the analysis of spectral flux measurements from extended structures that scatter X-ray radiation originating from point-like sources.

In Fig. 4: Top Left is the baseline phantom (normal oxygen level); Top Center is phantom with a local oxygen deficiency (15% reduction); Top Right is differential sinogram ΔI recorded by lateral detectors. Bottom Left – reconstruction using a SIRT-like method (without filtering); Bottom Center – reconstruction after Total Variation (TV) regularization (the anomaly becomes sharper and more compact); Bottom Right – ground-truth hypoxia mask.

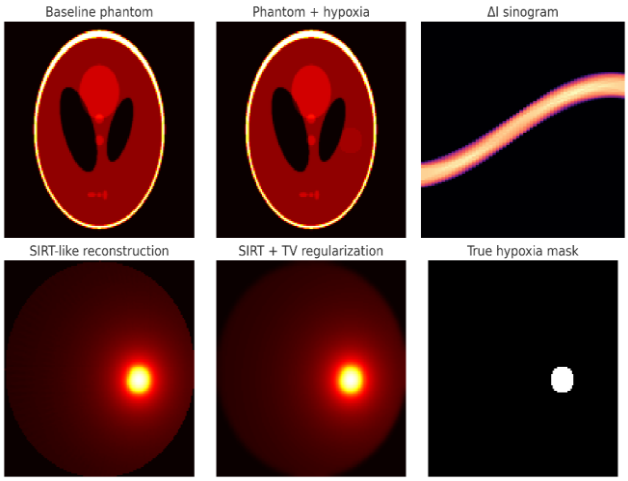

Figure 4: Mapping of a 2D Chemical Inhomogeneity (Shepp-Logan).

The Fig. 4 demonstrates that a local chemical anomaly is successfully recovered as a bright region, even for a weak perturbation (+15%). TV regularization significantly improves spatial localization.

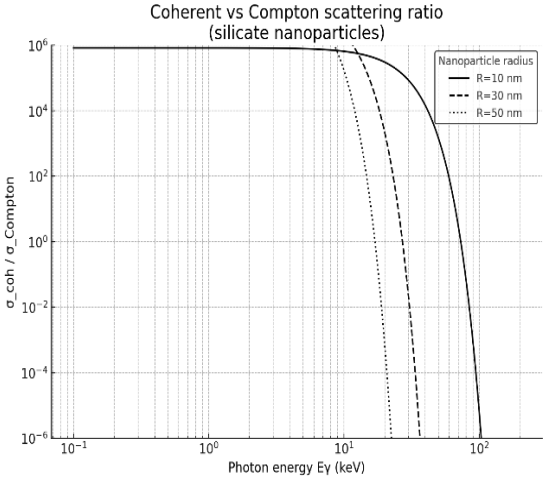

Figure 5: Relative contribution of Compton-type scattering for nanoparticles.

The Fig. 5 demonstrates that a local chemical anomaly is successfully recovered as a bright region, even for a weak perturbation (+15%). TV regularization significantly improves spatial localization.

Discussion. In the coming years, the deployment of next-generation (third-generation) detector-spectrographs is anticipated. The crystals used in these detectors possess a complex spatial structure, imposing constraints on the dimensions of the elementary pixel cells. For applications in X-ray and soft γ-ray spectroscopy, it is essential that the voxel length be no less than 1 cm, while the pixel width should not exceed several tens of nanometers. A potential difference of up to 1000 V is applied across the voxel faces. Therefore, studying the degradation mechanisms of semiconductors incorporating heavy elements is of significant interest.

Materials such as CsPbBr perovskites (Doikov D. & Doikov M., 2024; Liu, Wu, Wei, 2022) fall into this category. In third-generation detectors, the spectra of high-energy radiation are recorded within each voxel. In light of the discussed challenges, the availability of detailed spectra of both scattered and characteristic radiation enhances the resolution of structures with chemical inhomogeneities. At the same time, the likelihood of artifact formation is reduced. In $CsPbBr_3$ semiconductors, the signal-to-noise ratio has reached values of 2–3%, which improves reconstruction quality and expands the capabilities of spectral imaging.

Spectral image reconstruction requires careful use of existing tools. In essence, the method is based on the analysis of scattered high-energy radiation and the reconstruction of object structures from their scattering signatures. Due to the well-known expression for the scattering indicatrix $p_{KN}\ \ \theta$ each atomic species exhibits a characteristic angular distribution that relates the photon scattering angle to its post-collision energy. In other words, the dispersion of the scattered radiation is directly linked to the chemical composition of the medium.

Color Indices. In some cases, the intensity of scattered high-energy radiation is too low to allow for detailed spectral reconstructions. For such scenarios, we propose using integrated flux ratios across selected spectral intervals, analogous to color indices in optical astronomy. In stellar spectroscopy, these color indices have shown sensitivity – and in some cases even correlation – with the metal content of stellar atmospheres. A similar approach may enhance the interpretability of scattering-based chemical imaging.

Spectral Geometry. The reconstruction of investigated objects using spectral analysis enables the extraction of additional structural and compositional details, which are directly related to the medium's radiative response to external irradiation. During the reconstruction process, both artifacts and zones with local physicochemical heterogeneities begin to emerge clearly, as illustrated in Fig. 4, thereby expanding the diagnostic potential of the proposed method.

6. Conclusion

Image reconstruction of irradiated media–based on the analysis of both transmitted and scattered radiation–has necessitated the development of new physical concepts, instrumentation strategies, and computational algorithms. This study substantiates the importance of incorporating scattered radiation into the image reconstruction framework. Contrary to the common belief that scattering leads only to image degradation and loss of diagnostic value, our results demonstrate that certain spectral regions actually provide "clean" dominance of specific interactions:

- Pure absorption: 0.1–10 keV;
- Pure scattering (mainly Compton): 40–160 keV;
- Competitive regime (absorption and scattering): 10–40 keV.

To simplify interpretation and facilitate visualization, we selected both liquid and solid phases of the most abundant cosmic and planetary environments: water and methane for planetary atmospheres, and silicates and carbonates for the interstellar medium. To date, most image reconstructions have been carried out under the pure absorption approximation, which assumes the radiation source is positioned behind the irregular medium along the source–detector axis. In this setup, the projection data corresponds to a 2D distribution of the absorption coefficient $\mu_a\,(x,y)$, which is commonly interpreted as the mass density map ρ_a (x,y). However, our findings indicate that such a configuration limits the amount of physical information retrievable from the system and often reduces irregularities to the level of noise in the detector image, thereby compromising contrast.

In regions corresponding to very small scattering angles $\theta \ll 1$, contrast loss due to scattering becomes significant and calls for additional mathematical treatment to restore interpretability. In cases where the effective number of scatterers (atoms) remains within the single-scattering regime (see equation (6)), our study demonstrates that it is feasible to reconstruct spatial distributions of the scattering coefficient $\mu_s(x,y)$ based on scattered radiation. This approach dramatically expands the observable volume–both geometrically and physically – compared to absorption-only techniques. Interestingly, such effects have also been observed by X-ray satellites, even in energy domains typically dominated by absorption. In these observations, nanoparticles of silicates and carbonates serve as primary scattering agents. However, under these conditions, scattering is primarily diffraction-based, governed by the macroscopic properties of the dust particles. Specifically, it depends on the refractive index in the X-ray regime, which is typically very close to unity. X-ray observatories have recorded diffraction halos around novae during their peak brightness phases (Drine, 2003). To quantify the contributions of diffraction and Compton scattering, the following spectral classification is applied:

- Soft X-ray halos (0.1–10 keV) dominated by diffraction (coherent scattering, σ_{coh} tipe);
- Intermediate range (10–40 keV) competitive regime (diffraction and Compton scattering);
- Hard X-rays (>40 keV) dominated by Compton scattering.

For an individual particle containing N electrons, the scattering cross section must be computed accordingly to capture the contributions of both coherent and incoherent processes.

$$\frac{\sigma_{coh}}{\sigma_{Compt}} \approx \frac{N^2 |F\ q\ |^2}{N\sigma_{KN}} \tag{16}$$

$$|\,F(q)\,|^2 \approx exp\,-\,qR^{\,2}\,, q = \frac{4\pi}{\lambda}\sin\theta/2 \tag{17}$$

For the first time, previously invisible shells near novae have been identified based on scattered radiation. We have determined a wavelength interval in which diffraction-based X-ray scattering by dust becomes comparable to–or even exceeds – Compton scattering. By comparing the angular scattering indicatrices associated with the two mechanisms, $\mathrm{p_{KN}}(\theta_s)$ we found that $\mathrm{p_{KN}}(\theta_s)$ weaker anisotropy compared to the strongly forward-peaked, needle-like form of $\kappa\ \mathrm{p}_{Difr}(\theta_s)$. The sharp angular structure of $\kappa\ \mathrm{p}_{Difr}(\theta_s)$. makes it particularly suitable for both forward and inverse Radon transform techniques.

Author Contributions: D.D. developed the physical model presented in Section 2-4. The *Introduction*, problem Formulation, *Discussion*, and *Conclusion* were co-written.

References

Bracewell R.N., Riddle A.C.: 1967, *Astroph. J.*, **150**, 427. DOI: 10.1086/149346

Chevalier R.A., Fransson C.: arXiv.1612.07459v1 [astro-ph.He], 22 Dec 2016.

Costantini E., Corrales L.: 2022, aanda.org+5edoc.ub.uni-muenchen.de+5cxc.harvard.edu+5arXiv.

Doikov M.: 2024, *OAP*, **37**, 11-14. DOI: 10.18524/1810-4215.2024.37.312675

Doikov D.N., Doikov M.D.: 2024, *OAP*, **37**, 5-10. DOI: 10.18524/1810-4215.2024.37.312680

Draine B.T.: 2003, aanda.org+15cxc.harvard.edu+15arXiv+15.

Jerkstrand A., Fransson C., Kozma C.: 2011, *A&A*, **530**, A45, 1-23.

Lee J.C.: 2011, *Space Sci. Rev.*, **157**, 93–101. https://doi.org/10.1007/s11214-010-9723-2

Liu Fangze, Wu Rong, Wei Jing, Ni Wanyi et. al.: 2022, *ACS Energy Lett.*, **7**, 1066–1085, https://doi.org/ 10.1021/acsenergylett. 2c00031.

The Physics of Medical Imaging: 1991 / Ed. by Steve Webb. IOP Publishing Ltd. pp. 138-171.